solids

MDPI

Article

An Electron Waveguide Model for FDSOI Transistors

Ulrich Wulf

Department of Computational Physics, Brandenburg Technical University Cottbus/Senftenberg, P.O. Box 101344, 03013 Cottbus, Germany; ulrich.wulf@b-tu.de; Tel.: +49-355-69-3061

Abstract: We extend our previous semi-empirical model for quantum transport in a conventional nano-MOSFET to FDSOI transistors. In ultra-thin-body and -BOX (UTBB) FDSOI transistors, the electron channel can be treated as an electron waveguide. In the abrupt transition approximation, it is possible to derive an analytical approximation for the potential seen by the charge carriers. With these approximations we calculate the threshold voltage and the transfer characteristics, finding remarkably good agreement with experiments in the OFF-state given the relative simplicity of our model. In the ON-state, our theory fails because Coulomb interaction between the free charge carriers and the device heating is neglected in our approach.

Keywords: nanotransistor; electron wave guide; FDSOI transistor; quantum transport

Citation: Wulf, U. An Electron Waveguide Model for FDSOI Transistors. *Solids* **2022**, *3*, 203–218. https://doi.org/10.3390/solids3020014

Academic Editor: Antonio Polimeni

Received: 27 February 2022
Accepted: 6 April 2022
Published: 15 April 2022

1. Introduction

The notion of electron waveguide transport was used in the late 1980s and in the 1990s to discuss split-gate AlGaAs/GaAs devices [1,2]. The initiating observation in this field was the observation of quantized conduction in a point contact [3,4]. The electron waves in the waveguide are the quantum mechanical wave functions resulting from the Schrödinger equation, which are assumed to be coherent in the entire device. In a wave guide, transport is subjected to a two-dimensional potential perpendicular to the transport direction and leading to global transverse modes. Here we present a model for a FDSOI transistor in which its conduction channel is treated as an electron waveguide (FD—fully depleted, SOI—silicon-on insulator; for a review, see [5]). The model is formulated so that it can be generalized to other modern transistor architectures such as FinFETs, horizontal and vertical Nanowire transistors, and Nanosheet FETs in which the conduction channel takes a similar form [6].

For the transverse modes of an electron waveguide to be observable, essentially three conditions have to be fulfilled [2]: (i) The scale of the transverse confinement must be at most comparable to the Fermi wave length; (ii) The dimensions of the conduction channel have to be smaller than the elastic and inelastic scattering lengths; and (iii) The differences of the energies of the transverse modes must be larger than the thermal energy and larger than eU_D, where U_D is the applied drain voltage.

In a series of studies [7–10], we developed a compact semi-empirical model for quantum transport in a conventional nano-MOSFET in which the experimental output characteristics could be described quantitatively. In this study, we extend this model to thin body transistors focusing on ultra-thin-body and -BOX (UTBB) FDSOI transistors with a back plane (BP) as a back gate [5,11–19]. Typically, in a UTBB FDSOI transistor the threshold voltage (VT) is adjusted by the work function of the metal gate, the polarity of the BP-doping, and the back gate bias allowing multi-VT operation [5,18]: High-VT (HVT) devices allow for low-leakage currents and low power dissipation whereas standard-VT (SVT) and low-VT (LVT) devices allow for fast operation. Because of the ultra-thin-body it is possible to define in the considered devices global transverse modes without mode coupling, thus simplifying more complex T-matrix type approaches with inherent mode coupling as in References [20–25].

In general, Coulomb interaction between the free charge carriers and device heating play an important role in thin film devices [26–31]. However, here we focus on the threshold- and sub-threshold regime which are of particular importance for CMOS-technology. Therefore, we may neglect these effects. It is thus possible to derive an analytical understanding of a number of the aspects of the transistor. Compared to experiments by [18], we find reasonable agreement. We also discuss to what extent the electron waveguide conditions i–iii are met in the considered UTBB FDSOI transistors.

2. Materials and Methods

2.1. Quantum Transport Model

We consider a multiple VT, fully depleted SOI-transistor with a back plane (BP), as depicted in Figure 1. The n-conduction channel (waveguide) is located in a thin, nearly undoped active Si-layer of thickness D ('thin body') and width W. The conduction channel is sandwiched between the source- and the drain contact, which are heavily n-doped. The bottom side of the active Si-layer is terminated by an insulating SiO_2-layer (BOX). Below lies the BP consisting either of a heavily p- or a heavily n-doped silicon layer. The back contact with voltage U_{BG} is connected to the BP via a p-doped region ('p-well'). Further abbreviations are HK-MG for the high-k/metal gate stack and STI for shallow trench insulation. Outside the active Si-layer, the wave functions of the current carrying electrons vanish, leading to the boundary condition

$$\Psi(x, y = 0, z, E) = \Psi(x, D, z, E) = \Psi(x, y, 0, E) = \Psi(x, y, W, E) = 0 \tag{1}$$

(Definition of the coordinates. Figure 1b.) In the active layer with (100)-orientation (Figure 1d), we start from the single particle Schrödinger equation

$$\left[-\frac{\hbar^2}{2m_x^\alpha}\frac{\partial^2}{\partial x^2} - \frac{\hbar^2}{2m_y^\alpha}\frac{\partial^2}{\partial y^2} - \frac{\hbar^2}{2m_z^\alpha}\frac{\partial^2}{\partial z^2} + V(x,y) - E \right] \Psi(\vec{r}, E) = 0. \tag{2}$$

Here we assume isotropy in the z-direction (width direction). In the bulk semiconductor there are six equivalent valleys $\alpha = 1 \ldots 6$, which in the finite Si-layers are split into three classes (Figure 1): First $\alpha = 1, 2$ with $m_x^{1,2} = m_\parallel$, $m_y^{1,2} = m_z^{1,2} = m_\perp$, second, $\alpha = 3, 4$ with $m_x^{3,4} = m_z^{3,4} = m_\perp$, $m_y^{3,4} = m_\parallel$, and, third, $\alpha = 5, 6$ with $m_x^{5,6} = m_y^{5,6} = m_\perp$, $m_z^{5,6} = m_\parallel$. Here $m_\parallel = 0.91 m_0$ is the large effective mass and $m_\perp = 0.19 m_0$ is the small effective mass associated with the constant energy ellipsoids of the valleys.

If the thickness of the Si-layer is small, one can approximate $V(x, y)$ by its average $\bar{V}(x)$ defined by

$$V(x,y) \to \bar{V}(x) = \frac{1}{D}\int_0^D dy V(x,y) \tag{3}$$

so that

$$\left[-\frac{\hbar^2}{2m_x^\alpha}\frac{\partial^2}{\partial x^2} - \frac{\hbar^2}{2m_y^\alpha}\frac{\partial^2}{\partial y^2} - \frac{\hbar^2}{2m_z^\alpha}\frac{\partial^2}{\partial z^2} + \bar{V}(x) - E \right] \Psi(\vec{r}, E) = 0 \tag{4}$$

(see Figure 2b,c). Because of good screening in the contacts we can write $V(x < 0, y) = 0$ and $V(x \geq L, y) = -eU_D$ leading to

$$\bar{V}(x > L) = 0 \quad \text{and} \quad \bar{V}(x \geq L) = -eU_D. \tag{5}$$

The effective potential in the scattering area $\bar{V}(0 \leq x \leq L)$ will be discussed in Section 2.2. The independence of the potential (4) of the transverse coordinates allows for a product ansatz

$$\Psi(\vec{r}, E) = \psi(x, E^x)\Phi_n(y, z) \tag{6}$$

for the wave functions which correspond to electron states in an electron wave guide. Here the global transverse modes are given by

$$\Phi_n = \Phi_{n_y n_z} = \frac{2}{\sqrt{DW}} \sin\left(n_y \frac{\pi}{D} y\right) \sin\left(n_z \frac{\pi}{W} z\right). \tag{7}$$

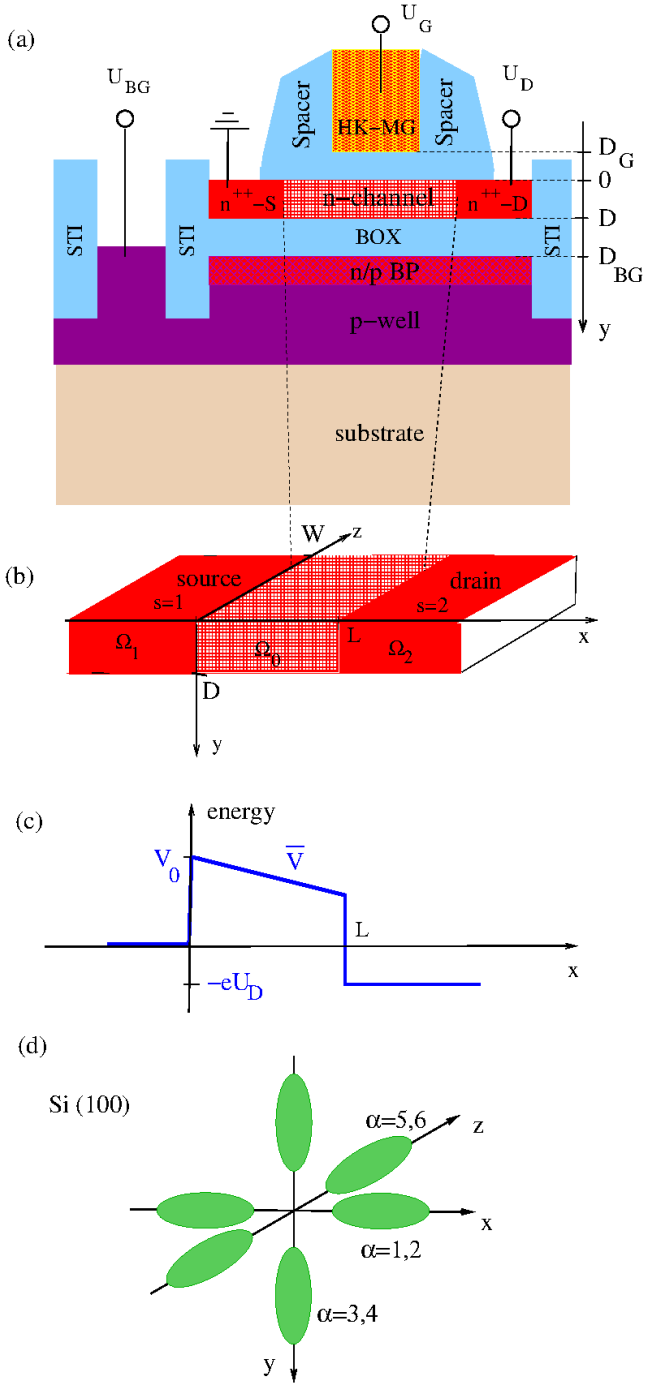

Figure 1. (**a**) N-channel multiple VT, fully depleted SOI-transistor with a back plane (BP) (see text). (**b**) Active Si-layer for the conduction channel taking the form of a waveguide. (**c**) One-dimensional effective potential $\bar{V}$ after Equation (22). (**d**) The (100)-orientation of the active Si-layer with the six constant energy ellipsoids $\alpha = 1 \ldots 6$.

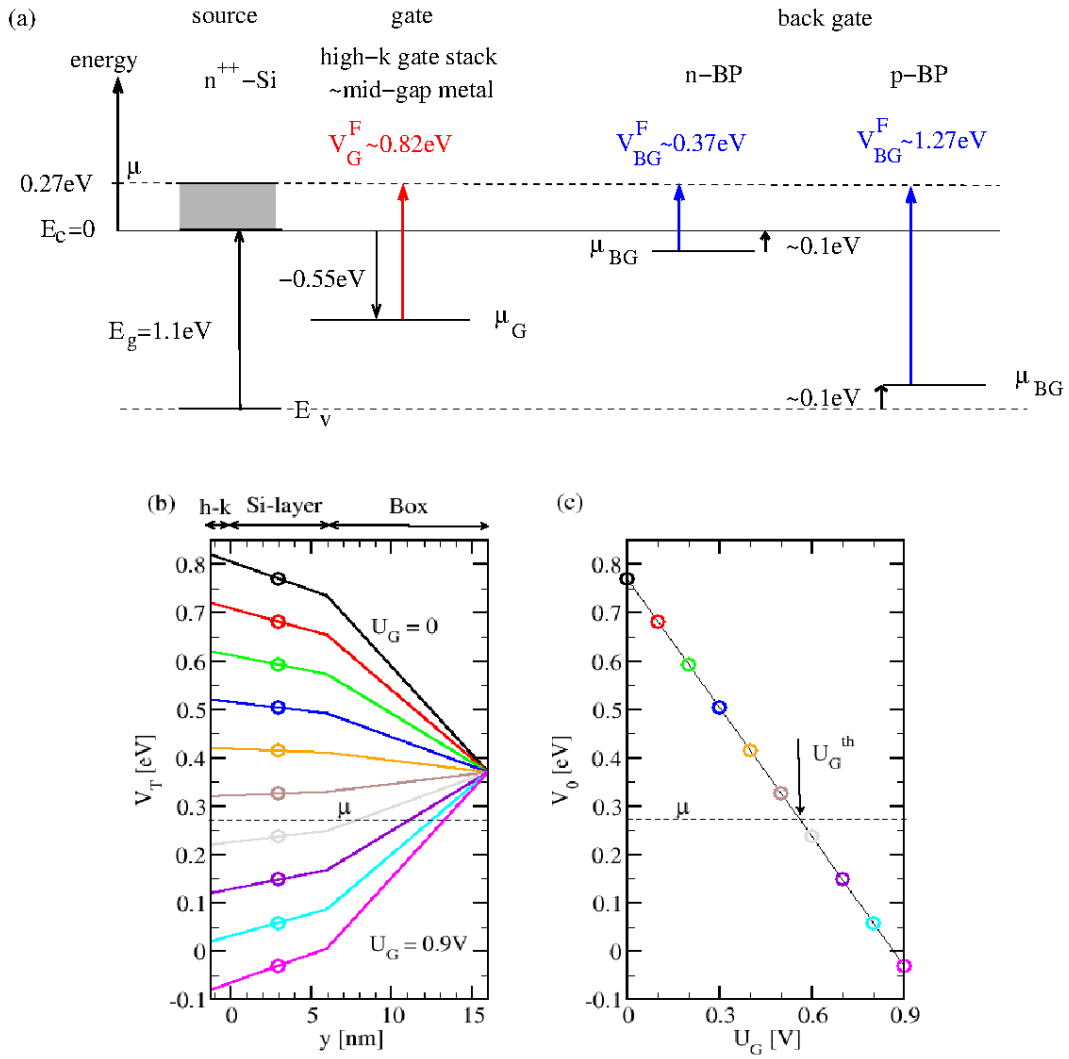

Figure 2. For the theoretical parameter set listed at the beginning of Section 3: (**a**) Energy diagrams of the isolated contacts. (**b**) Transverse confinement potential $V_T(y)$ for an n-BP at $U_{BG} = 0$ (SVT(i)) for U_G = 0.0 (black), 0.1 V (red), 0.2 V (green), 0.3 V (blue), 0.4 V (orange), 0.5 V (brown), 0.6 V (grey), 0.7 V (violet), 0.8 V (cyan), and 0.9 V (magenta). (**c**) In circles: Effective barrier height V_0 resulting from Equation (33), color coding as in part (**b**). Marked by an arrow: Threshold gate voltage U_G^{th} determined by condition (39).

The factor $\psi(x, E^x)$ describes the propagation of a charge carrier in this mode since the total energy E is split in a transverse energy of the motion in the y-z-direction

$$E_n^\perp = E_{n_y n_z}^\perp = \frac{\hbar^2}{2m_y^\alpha}\left(n_y \frac{\pi}{D}\right)^2 + \frac{\hbar^2}{2m_z^\alpha}\left(n_z \frac{\pi}{W}\right)^2 \tag{8}$$

and a longitudinal energy

$$E^x = E - E_n^\perp \tag{9}$$

of the motion in the x-direction. Insertion of (6) into (4) leads to the one-dimensional scattering problem

$$\left[-\frac{\hbar^2}{2m_x^\alpha}\frac{d^2}{dx^2} + \bar{V}(x) - E^x\right]\psi(x, E^x) = 0. \tag{10}$$

The source-incident scattering solutions $\psi^1(x, E^x)$ exhibit the asymptotic

$$\psi^{1\alpha}(x \leq 0, E^x) = e^{ik_{1\alpha}x} + r^{1\alpha}(E^x)e^{-ik_{1\alpha}x} \tag{11}$$

and

$$\psi^{1\alpha}(x \geq L, E^x) = t^{1\alpha}(E^x)e^{ik_{2\alpha}(x-L)}. \tag{12}$$

Here the wave number is given by

$$k_{ns\alpha}(E) = \sqrt[+]{\frac{2m_x^\alpha}{\hbar^2}(E - E_\perp^n + eU_s)} = \sqrt[+]{\frac{2m_x^\alpha}{\hbar^2}(E^x + eU_s)} \equiv k_{s\alpha}(E^x) \tag{13}$$

with $s = 1$ for the source and $s = 2$ for the drain as well as $U_1 = 0$ and $U_2 = U_D$. Our method for the numerical evaluation of the transmission coefficients $t^{1\alpha}$ is described in detail in Appendix E of [10].

The drain current results from the contributions of the six valleys according to $I_D = \sum_\alpha I_D^\alpha$ given by the Landauer–Büttiker formula. As we discuss in detail in Appendix A:

$$I_D^\alpha = \frac{2e}{h}\int_0^\infty dE^x [S_\alpha(E^x - \mu) - S_\alpha(E^x - \mu + eU_D)]\tilde{T}^{1d}(E^x). \tag{14}$$

Here the one-dimensional current transmission is given by

$$\tilde{T}^{1d}(E^x) = k_{2\alpha}(E^x)|t^{1\alpha}(E^x)|^2 k_{1\alpha}(E^x)^{-1}. \tag{15}$$

In the limit of large W, the supply function is given by

$$S_\alpha(\beta) = W\sqrt{\frac{m_z^\alpha k_B T}{2\pi\hbar^2}}\sum_{n_y} F_{-1/2}\left[-\frac{1}{k_B T}\left(\beta + n_y^2\frac{\pi^2\hbar^2}{2m_y^\alpha D^2}\right)\right] \tag{16}$$

with the Fermi–Dirac integral

$$F_j(x) = \frac{1}{\Gamma(j+1)}\int_0^\infty dy \frac{y^j}{1 + e^{y-x}}. \tag{17}$$

The calculation of the chemical potential μ is demonstrated in Appendix B. The total current per width is determined from (14) according to

$$J = \frac{I_D}{W} = \frac{1}{W}\sum_\alpha I_D^\alpha. \tag{18}$$

2.2. Potential in Abrupt Transition Approximation

For the potential in the Si-film entering into (2), we can write in the contacts $V(x < 0, 0 \leq y \leq D) = 0$ and $V(x > L, 0 \leq y \leq D) = -eU_D$. In the conduction channel, i.e., for $0 \leq x \leq L$ it can be found from Poisson's equation

$$\left(\frac{\partial^2}{\partial x^2} + \frac{\partial^2}{\partial y^2}\right)V(x, y) = \frac{e}{\kappa_0\kappa(y)}\rho(x, y) \tag{19}$$

with the charge density ρ and appropriate boundary conditions. Here, κ_0 is the vacuum permitivity and $\kappa(-D_G < y < 0)$ is given by the dielectric constant κ_{HK} of the high-k-dielectric, $\kappa(0 \leq y \leq D)$ is given by the dielectric constant κ_{Si} of the Si-film, and $\kappa(D < y \leq D_{BG})$ is given by the dielectric constant κ_{Ox} in the BOX. As shown in Figure 1a, $y = -D_G$ marks the interface between top-gate insulation and top gate and $y = D_{BG}$ marks the interface between BOX and back gate (BP). For the conduction channel, we specialize Equation (19) to the threshold- and sub-threshold regime, which is important

for technological applications. Here, we may neglect the contribution of the free charge carriers. In FDSOI technology, one assumes furthermore the full ionization of the impurities (depletion approximation) so that $\rho = -eN_A\Theta(y)\Theta(D-y)$ with the acceptor density N_A in the Si-layer. One finds

$$\left(\frac{\partial^2}{\partial x^2}+\frac{\partial^2}{\partial y^2}\right)V(x,y) = -\frac{e^2}{\kappa_0\kappa(y)}N_A\Theta(y)\Theta(D-y)N_A. \tag{20}$$

This equation was studied, e.g., in References [32–36]. To construct a potential approximation of the form $\bar{V}(x)$ as assumed in Equation (4), we here apply the *abrupt transition*-approximation as described in References [9,10]. While in the contacts we have $V(x \le 0, y) = 0$ and $V(x \ge L, y) = -eU_D$, there is an abrupt transition to the potential in the scattering area ($0 < x < L$, conduction channel). In the scattering area, we seek a solution of (20) of the separable form

$$V(0 \le x \le L, y) = -eU_D\frac{x}{L} + V_T(y) \tag{21}$$

and then construct according to (3)

$$\bar{V}(x) = \frac{1}{D}\int_0^D dy\left[-eU_D\frac{x}{L} + V_T(y)\right] = V_0 - eU_D\frac{x}{L}. \tag{22}$$

In the latter expression we assume for a thin film that the quantization energy induced by the boundary condition $\Psi(x, y = 0, z, E) = \Psi(x, D, z, E)$ is dominant over the potential variation of $V_T(y)$ so that we can replace $V_T(y)$ with its average, $V_0 = (1/D)\int_0^D dy V_T(y)$. Upon insertion of (21) into (20), one obtains

$$\frac{d^2}{dy^2}V_T(y) = -\frac{e}{\kappa_0\kappa(y)}N_A\Theta(y)\Theta(D-y). \tag{23}$$

We now impose Dirichlet boundary conditions

$$V_T(-D_G) = -eU'_G = -eU_G + V_G^F \quad \text{and} \quad V_T(D_{BG}) = -eU'_{BG} = -eU_{BG} + V_{BG}^F. \tag{24}$$

As usual, the flat band energies

$$V_G^F = \mu - \mu_G \quad \text{and} \quad V_{BG}^F = \mu - \mu_{BG} \tag{25}$$

are defined by the difference between the chemical potential in the grounded source μ and the chemical potential in the respective isolated contact, μ_G for the top gate and μ_{BG} for the back gate. Then, one has for the electro chemical potential in the top gate for $U_G = 0$ the value $\mu_G + V_T(-D_G) = \mu_G + V_G^F = \mu$ as required. Furthermore, we require at the two silicon-insulator interfaces at $y = 0$ and $y = D$ the usual continuities of V_T and $\kappa V'_T$, resulting in

$$V_T(0^-) = V_T(0^+) \quad \text{and} \quad \kappa(0^-)\frac{d}{dy}V_T\big|_{0^-} = \kappa(0^+)\frac{d}{dy}V_T\big|_{0^+} \tag{26}$$

plus corresponding relations at $y = D$. As is characteristic for the *abrupt transition*-approximation, the potential in (21) can be interpreted as the superposition of, first, a constant electric field in longitudinal direction, $E_x = -U_D/L$, induced by the drain voltage and, second, a transverse potential variation $V_T(y)$ describing an infinite conduction channel at $U_D = 0$.

The reduced Poisson equation (23) with the boundary conditions (24) can be solved easily with the ansatz

$$V_T(y < 0) = c_1(y + D_G) - eU'_G, \tag{27}$$

$$V_T(0 \le y \le D) = -\frac{C}{2}y^2 + \alpha y + \beta \tag{28}$$

with $C = e^2 N_A/(\kappa_0 \kappa_{Si})$, and

$$V_T(y > D) = c_2(y - D_{BG}) - eU'_{BG}. \tag{29}$$

In Appendix C we show

$$\alpha = \frac{CD^2/2 + \kappa_2 C D D_{Box} + e(U'_G - U'_{BG})}{D + \kappa_2 D_{Box} + \kappa_1 D_G} \tag{30}$$

as well as

$$\beta = \kappa_1 \alpha D_G - eU'_G, \tag{31}$$

with $\kappa_1 = \kappa_{Si}/\kappa_{HK}$, $\kappa_2 = \kappa_{Si}/\kappa_{Ox}$, and $D_{Box} = D_{BG} - D$. Furthermore,

$$c_1 = \kappa_1 \alpha \quad \text{and} \quad c_2 = -\frac{-CD^2/2 + \alpha D + \beta + eU'_{BG}}{D_{Box}}. \tag{32}$$

From Equations (3), (21) and (22) one finds for the barrier height

$$V_0 = \frac{1}{D}\int_0^D dy \left[-\frac{C}{2}y^2 + \alpha y + \beta\right] = -\frac{C}{6}D^2 + \frac{\alpha}{2}D + \beta. \tag{33}$$

3. Results

Theoretical parameters: With the exception of Figure 3 where we vary the parameter D_{Box}, we use the parameters $D_G = 1.2$ nm, $D = 6$ nm, $D_{Box} = 10$ nm, $\kappa_{Si} = 12$, $\kappa_{Ox} = 3.9$, $\kappa_{HK} = 12$ (D_G is the equivalent oxide thickness EOT), $L = 30$ nm, $W \to \infty$, $T = 298$ K, $N_D = 5 \times 10^{20}$ cm^{-3} (n^{++}-doping in source and drain), $N_A = 10^{15}$cm^{-3} (weak p-doping in conduction channel), and the operating voltage of $U_{DD} = 0.9$ V. These parameters are compatible with the ones in Reference [18]. From Equation (A15), one obtains a value of $\mu \sim 0.27$ eV. As shown in the energy diagrams of the isolated contacts in Figure 2a, we take the bottom of the conduction band in the grounded n^{++}-source as the energy zero. For the chemical potential in the isolated gate metal, we choose $\mu_G = -0.55$ eV, which is the mid gap position in silicon. For the back gate one assumes a doping concentration markedly lower than that of the n^{++}-source ($\sim 10^{18}$ cm^{-3} in Reference [18]) corresponding to $\mu_{BG} = -0.1$ eV for an n-BP and $\mu_{BG} = -1.0$ V for a p-BP. For the flat band voltages, it follows from (25)

$$V_G^F = 0.82 \text{ eV}, \qquad V_{BG}^F = 0.37 \text{ eV} \quad \text{(n-BP)}, \quad \text{and} \quad V_{BG}^F = 1.27 \text{ eV} \quad \text{(p-BP)} \tag{34}$$

(See Figure 2a.) As an example, we consider in Figure 2 an n-channel transistor with an n-BP at $U_G = 0$. In part (b), the transverse potential $V_T(y)$ is plotted as calculated from Equations (27)–(29). In the limit of small D, it is permissible to set $C \to 0$ (for discussion, see Equation (A30)) so that in (28) the curvature of the potential in the conduction channel can be neglected. In consequence, $V_T(y)$ is close to a piecewise linear function across the silicon layer. The transverse ideal box-confinement induced by the boundary condition $\Psi(x, y = 0, z, E) = \Psi(x, D, z, E)$ in Equation (1) causes a typical quantization energy ΔE in the corresponding ideal box-confinement given by

$$\Delta E = \frac{\hbar^2}{2m*}\left(\frac{\pi}{D}\right)^2 = 32 \text{ meV}. \tag{35}$$

at $D = 6$ nm, were $m^* = (m_\perp * m_\parallel^2)^{1/3} = 0.32 m_0$ is the effective band mass. We compare this energy to the absolute value of the total change ΔV of V_T across the conduction channel as taken from Figure 2b. This change is maximum at $U_G = 0$, taking the value $\Delta V \sim 80$ meV. Therefore, $\Delta V \lesssim \Delta E < 3\Delta E$ holds, where $3\Delta E$ is the excitation energy from the first to

the second lowest level of the quantization in the y-direction. This relation justifies the transition from Equation (2) to Equation (4). Comparing ΔE to $k_B T \sim 25$ meV at room temperature, it is seen that condition (iii) for the observability of the transverse modes listed in the introduction is fulfilled. Setting $\mu \sim E_F = \hbar^2 k_F^2/(2m^*)$ and $\lambda_F = 2\pi/k_F$, one obtains $\lambda_F \sim 4$ nm. So condition (i) is almost fulfilled, especially if one takes smaller values for N_D. Condition (ii) probably requires shorter channels.

In Figure 2c, the effective barrier height V_0 according to Equation (33) is shown. In the limit $C \to 0$, one obtains a linear relation $V_0(U_G)$ given by

$$V_0 = V_0^0 - (1 - A)eU_G \tag{36}$$

with

$$V_0^0 = V_G^F + A(V_{BG}^F - V_G^F - eU_{BG}) \tag{37}$$

and

$$A = \frac{D/2 + \kappa_1 D_G}{D + \kappa_2 D_{Box} + \kappa_1 D_G} \tag{38}$$

(see Appendix D). Because $\kappa_2 D_{Box} \gg D, \kappa_1 D_G$, the parameter A is small, for our system taking the value $A = 0.12$, so that $dV_0/dU_G \sim -1$.

In Figure 2c, we also plot the threshold voltage U_G^{th} (in text abbreviated with VT) as calculated from the condition

$$V_0(U_G^{th}) = \mu. \tag{39}$$

This condition was used in earlier studies for a conventional MOSFET (see, for example, Figure 4 of [9]).

An important feature of the FDSOI technology is the possibility to control the threshold gate voltage, first, by choosing either an n-BP or a p-BP, and, second, by applying a voltage U_{BG} at the BP. Important VT-options are listed in Table 1 of [16]:

1. n-BP with $U_{BG} = 0$: standard-VT (SVT (i)), identical with Figure 2b;
2. n-BP with $U_{BG} = U_{DD}$: low-VT (LVT);
3. p-BP with $U_{BG} = 0$: high-VT (HVT);
4. p-BP with $U_{BG} = U_{DD}$ standard-VT (SVT (ii)).

The associated effective barrier heights V_0 are given in Figure 4. From Equation (36), one finds in all four cases a good linear approximation $V_0(U_G)$ with identical slopes ~ -1. A further inspection of Equation (36) reveals that equal barrier heights for SVT(ii) and SVT(i) result from the identical value $V_{BG}^F - eU_{BG} = 0.5eV$. In the general case, one obtains identical results for SVT(i) and SVT(i) if

$$\Delta V_{BG}^F = e\Delta U_{BG} = U_{DD} \tag{40}$$

where ΔV_{BG}^F is the difference between the flat band energies in the p-BP and the n-BP.

In Figure 3, we plot the threshold voltage calculated from condition (39) with the linear approximation of $V_0(U_G)$, as given in Equation (36) so that

$$eU_G^{th} = \frac{V_0^0 - \mu}{1 - A}. \tag{41}$$

We find reasonable agreement with the experimental results in Figure 3 of [18]. In Appendix D, it is shown that (41) can be simplified to give

$$eU_G^{th} \sim -\mu_G + \frac{D/2 + \kappa_1 D_G}{\kappa_2 D_{Box}}(-\mu_{BG} - eU_{BG}). \tag{42}$$

In Figure 3 it is demonstrated that the expressions (41) and (42) agree very closely. According to Equation (42), we find for $D_{Box} \to \infty$ the value for $U_G^{th,\infty} = -\mu_G = 0.55$ corresponding to mid-gap position. From Figure 3 of [18], we read for $D_{Box} \to \infty$ the

experimental value $U_G^{th,\infty} = 400$ mV, which might indicate a shift of the experimental μ_G from mid-gap position. The formula (42) explains the finding $eU_G^{th} + \mu_G \propto 1/D_{Box}$, which is present in experiments as well. Note that in theory and experiments, the identical curves for SVT(i) and for SVT(ii) both bend up slightly.

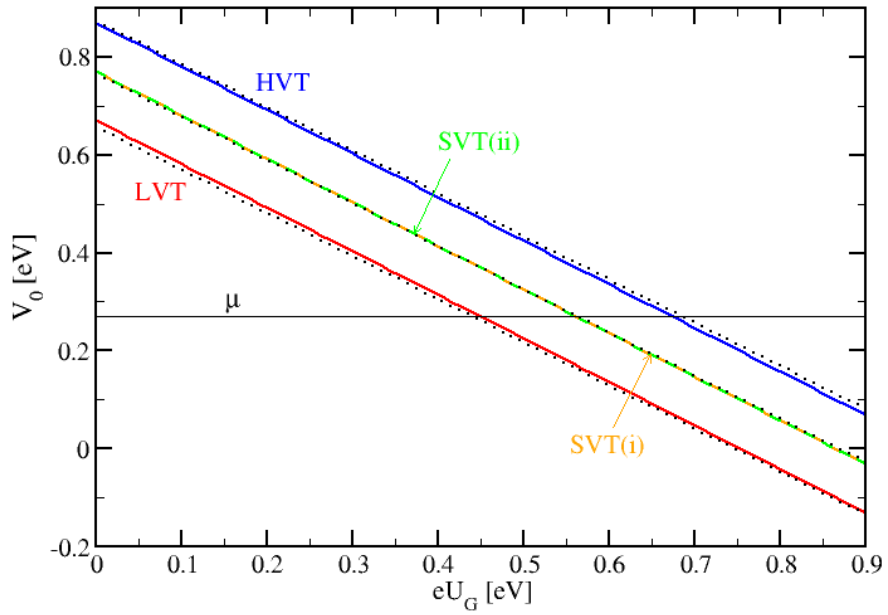

Figure 3. The threshold voltage versus thickness of the box: n-BP with $U_{BG} = 0$ (orange), n-BP with $U_{BG} = U_{DD}$ (red), p-BP with $U_{BG} = 0$ (blue), and p-BP with $U_{BG} = U_{DD}$ (green). Solid lines according to Equation (41) and dashed lines according to Equation (42). The circles mark the values for $D_{Box} = 10$ nm which enter Table 1.

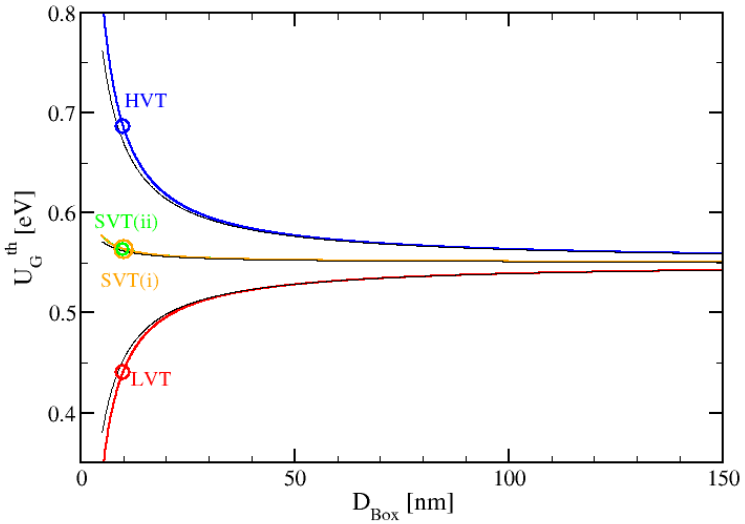

Figure 4. For the system parameters, the barrier height $V_0(eU_G)$ from (33): n-BP with $U_{BG} = 0$ (SVT(i), orange), n-BP with $U_{BG} = U_{DD}$ (LVT, red), p-BP with $U_{BG} = U_{DD}$ (SVT(ii), green), and p-BP with $U_{BG} = 0$ (HVT, blue). In dotted black lines: Linear approximation to $V_0(eU_G)$ in Equation (36). The horizontal black solid line marks the chemical potential μ where the intersection points with $V_0(eU_G)$ give the threshold voltage U_G^{th}, according to (39).

In Figure 5 we plot the transfer characteristics resulting in the four VT-options. As documented in Table 1, we find for the threshold- and subthreshold regime a remarkable agreement between theory and experiment in view of the simplifications in our theory. The major simplifications are the use of the abrupt transition approximation, the neglect of

Coulomb interaction of the free carriers, and the disregard of the x-dependence of V_T. It can be expected that without abrupt transition approximation, the transition between contacts and conduction channel is smoothed out and the maximum of the barrier is shifted from $x = 0$ towards the interior of the conduction channel. Because of the longitudinal electric field in the conduction channel, the height of the barrier will then be reduced, leading to the well-known *drain induced barrier lowering* (DIBL). This effect can explain the higher theoretical values for I_{OFF}. As can be expected, in the ON-state our model fails. The first reason is the neglect of the free carriers in the charge density entering into the Poisson equation (20). Above threshold free carriers increasingly enter the conduction channel and alter the potential because of screening. The second reason is heating, which has been neglected in our approach but which becomes substantial above threshold. The third reason is the neglect of the linear drop of V_T, which becomes important in the ON-state when $V_0 \sim 0$.

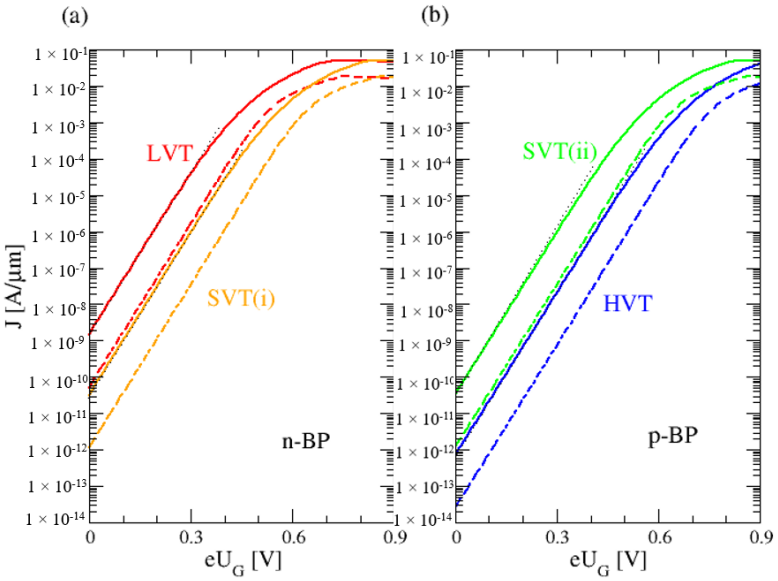

Figure 5. For theoretical parameters the transfer characteristics for $U_D = 0.05$ V (dashed lines) and $U_D = 0.9$ V (solid lines). (**a**) for a n-BP and (**b**) for a p-BP. Color coding as in Figure 3. In black: Traces taken to extract the SS.

Table 1. Electrical characteristics of multi-V_T nMOS-transistors: above theoretical values taken from Figures 3 and 5, below experimental values taken from TABLE 2 of Reference entering only experimental values as stated [18].

Type	U_G^{th} [mV]	I_{ON} [µA/µm]	I_{OFF} [pA/µm]	SS [mV/dec]
LVT	440	45,900	1474	70
SVT(i)	563	49,452	32	70
SVT(ii)	563	44,952	32	70
HVT(i)	686	39,385	0.7	70
LVT	278	480	2139	77
SVT(i)	429	332	16	76
SVT(ii)	430	333	17	77
HVT(i)	567	208	0.1	73

4. Discussion

The presented theoretical model for a FDSOI transistor has been designed on the one hand to be complex enough to enter all relevant physical parameters and on the other hand to be simple enough to allow for an analytical discussion as much as possible. It is designed

for the threshold- and sub-threshold regime. Here, the theoretical results are remarkably close to the experimental ones. The model fails completely in the ON-state regime. Here, Coulomb interaction between the charge carriers and device heating becomes important [9] as well as the linear drop in V_T. These have been neglected in our model and have to be included in future work.

Funding: This research received no external funding.

Data Availability Statement: Not applicable.

Conflicts of Interest: The author declares no conflict of interest.

Abbreviations

The following abbreviations are used in this manuscript:

MDPI	Multidisciplinary Digital Publishing Institute
DOAJ	Directory of open access journals
TLA	Three letter acronym
LD	Linear dichroism

Appendix A. Adoption of a Previous Transistor model for the Calculation of the Drain Current

The transistor model in Section 4 of Reference [10], including conditions P1–P6, can be directly applied to the model for an SOI-transistor in Section 2.1. The waveguide geometry of the conduction channel in Figure 1b is identical with the geometry in Figure 2b of [10]. The potentials in the source Ω_1 and in the drain Ω_2 are identical. The global transverse modes arise from the separable potential in Equation (21), identical with equations (35) and (36) The notation 'equation (...)' we use for equations is in Reference [10]. The further thin-film approximation in Equation (22) corresponds to the setting in equation (35) $V_T(y) = 0$ and $V_L(x) = \bar{V}(x)$. The single transverse mode approximation condition P7 is introduced in Section 3. Because of the simple form of the transverse potential V_T, one has in P5 the planarity in the two transverse directions so that two global transverse coordinates y and z exist and $\vec{r}_\perp = (y, z)$. The longitudinal coordinates are $z_1 = -x$ for the source and $z_2 = x - L$ for the drain. Because of $V_T(y) = 0$, the transverse functions ϕ_k in the conduction channel and the transverse functions in the contacts Φ_n in Reference [10] coincide, having identical transverse mode energies,

$$E_k^T = E_{k_y,k_z}^T = \frac{\hbar^2}{2m^*}\left[\left(\frac{k_y\pi}{D}\right)^2 + \left(\frac{k_z\pi}{W}\right)^2\right] = E_k^\perp. \tag{A1}$$

Combining Equations (11), (12), and (6), the asymptotics of the source-incident scattering function take the form

$$\Psi^{1n\alpha}(x \le 0, y, z, E) = \psi^{1\alpha}(x \le 0, E^x)\Phi_n(y, z) = e^{ik_{1\alpha}x}\Phi_n(y, z) \tag{A2}$$

and

$$\Psi^{1n\alpha}(x \ge L, y, z, E) = t^{1\alpha}(E^x)e^{ik_{2\alpha}(x-L)}\Phi_n(y, z). \tag{A3}$$

Comparing with Equation (4), we obtain the relation

$$S_{2n',1n}^{\alpha}(E) = t^{1\alpha}(E^x)\delta_{nn'}. \tag{A4}$$

Then, from Equation (8) one obtains the current transmission sum

$$\begin{aligned} T_{21} &= \sum_n \Theta(E - E_n^{\perp} + eU_D)\Theta(E - E_n^{\perp}) k_{2\alpha}(E^x) k_{1\alpha}(E^x)^{-1} \left| t^{1\alpha}(E^x) \right|^2 \\ &= \sum_n \Theta(E^x) \tilde{T}^{1d}(E^x) \end{aligned} \tag{A5}$$

with the one-dimensional current transmission $\tilde{T}^{1d}$ given by Equation (15). From Equation (7), we find Equation (14)

$$\begin{aligned} I_D &= \frac{2e}{h} \sum_\alpha \int_{-\infty}^{\infty} dE [f(E-\mu) - f(E-\mu+eU_D) \sum_n \Theta(E^x) \tilde{T}^{1d}(E^x) \\ &= \frac{2e}{h} \sum_\alpha \int_0^{\infty} dE^x [S_\alpha(E^x - \mu) - S_\alpha(E^x - \mu + eU_D)] \tilde{T}^{1d}(E^x). \end{aligned} \tag{A6}$$

For $\beta = E^x - \mu$ or $\beta = E^x - \mu + eU_D$, the supply function is given by

$$\begin{aligned} S_\alpha(\beta) &= \sum_n f(\beta + E_\perp^n) = \sum_{n_y n_z} \left\{ \exp\left[\frac{1}{k_B T} \left(\frac{\hbar^2}{2m_y^\alpha} \frac{n_y^2 \pi^2}{D^2} + \frac{\hbar^2}{2m_z^\alpha} \frac{n_z^2 \pi^2}{W^2} + \beta \right) \right] + 1 \right\}^{-1} \\ &= W \sqrt{\frac{m_z^\alpha k_B T}{2\pi\hbar^2}} \sum_{n_y} F_{-1/2}\left[-\frac{1}{k_B T} \left(\beta + \frac{\hbar^2}{2m_y^\alpha} \frac{n_y^2 \pi^2}{D^2} \right) \right] \end{aligned} \tag{A7}$$

with the Fermi–Dirac integral

$$F_j(x) = \frac{1}{\Gamma(j+1)} \int_0^{\infty} dy \frac{y^j}{1 + e^{y-x}}. \tag{A8}$$

In the last step we made use of equations (70)–(73) occur in Reference [10] which hold in the limit $W \to \infty$. In the OFF-state, only the high-energy tail of the Fermi-distribution contributes significantly and a Boltzmann approximation can be introduced

$$F_j(x) \sim \frac{1}{\Gamma(j+1)} e^x \int_0^{\infty} dy y^j e^{-y} = e^x \tag{A9}$$

Appendix B. The Chemical Potential in Source and Drain

We assume identical cubic source/drain contacts of length $\mathcal{L}$ in the x-direction, D in the y-direction, and W in the z-direction. To calculate μ, we write the number of free charge carriers in the source contact

$$N = 2 \sum_{\alpha,n} \sum_{k_x} f\left(\frac{\hbar^2}{2m_x^\alpha} k_x^2 + E_n^{\perp} - \mu \right) = 2 \sum_\alpha \sum_{n_x n_z n_x = 1}^{\infty} f\left(\frac{\hbar^2}{2m_x^\alpha} \frac{n_x^2 \pi^2}{\mathcal{L}^2} + E_{n_y, n_z}^{\perp} - \mu \right), \tag{A10}$$

with $k_x = n_x \pi / \mathcal{L}$. Here, we assume fixed boundary conditions in all space directions and include spin degeneracy with a factor of two. Introducing the free carrier density n with $N = n\mathcal{L}DW$, one finds from (A10) in the limit $\mathcal{L} \to \infty$ and $W \to \infty$ setting $\sum_{n_x} .. \to (\mathcal{L}/\pi) \int dk_x \ldots$ and $\sum_{n_z} .. \to (W/\pi) \int dk_z \ldots$

$$1 = \frac{2}{N_D D} \sum_\alpha \sum_{n_y} \frac{1}{\pi^2} \int_0^{\infty} \int_0^{\infty} dk_x dk_z \frac{1}{\exp\left[\frac{1}{k_B T} \left(\frac{\hbar^2}{2m_x^\alpha} k_x^2 + \frac{\hbar^2}{2m_x^\alpha} k_z^2 + \frac{\hbar^2}{2m_x^\alpha} \frac{n_y^2 \pi^2}{D^2} - \mu \right) \right] + 1.} \tag{A11}$$

Here, we assume full ionization of the donors so that $n = N_D$ with the donor concentration N_D equal in source and drain. Define

$$X = \sqrt{\frac{\hbar^2}{2m_x^\alpha k_B T}} k_x, \qquad Z = \sqrt{\frac{\hbar^2}{2m_z^\alpha K_B T}} k_z, \quad \text{and} \quad R = \sqrt{X^2 + Z^2} \tag{A12}$$

to write

$$\begin{aligned} 1 &= \frac{2}{N_D D} \frac{1}{\pi^2} \sum_\alpha \sum_{n_y} \sqrt{\frac{2m_x^\alpha k_B T}{\hbar^2}} \sqrt{\frac{2m_z^\alpha k_B T}{\hbar^2}} \int_0^\infty dX \int_0^\infty dZ \frac{1}{\exp\left[X^2 + Z^2 + \frac{1}{k_B T}\left(\frac{\hbar^2}{2m_x^\alpha}\frac{n_y^2 \pi^2}{D^2} - \mu\right)\right] + 1} \\ &= \frac{2}{N_D D} \frac{1}{\pi^2} \frac{2k_B T}{\hbar^2} \sum_\alpha \sum_{n_y} \sqrt{m_z^\alpha m_x^\alpha} \int_0^\infty dR \frac{\pi}{2} R \frac{1}{\exp\left[R^2 + \frac{1}{k_B T}\left(\frac{\hbar^2}{2m_x^\alpha}\frac{n_y^2 \pi^2}{D^2} - \mu\right)\right] + 1}, \end{aligned} \tag{A13}$$

where we have included a quarter circle with radius R only. With $y = R^2 \Rightarrow dy = 2RdR$ it follows that

$$\begin{aligned} 1 &= \frac{1}{N_D D} \frac{1}{\pi} \frac{k_B T}{\hbar^2} \sum_\alpha \sqrt{m_z^\alpha m_x^\alpha} \sum_{n_y} \int_0^\infty dy \frac{1}{\exp\left[y + \frac{1}{k_B T}\left(\frac{\hbar^2}{2m_x^\alpha}\frac{n_y^2 \pi^2}{D^2} - \mu\right)\right] + 1} \\ &= \frac{1}{N_D D} \frac{k_B T}{\pi \hbar^2} \sum_\alpha \sum_{n_y} \sqrt{m_z^\alpha m_x^\alpha} \int_0^\infty dy \frac{1}{\exp(y - x) + 1} \end{aligned} \tag{A14}$$

with $x = [\mu - (\hbar^2/2m_x^\alpha)(n_y^2 \pi^2/D^2)]/k_B T$. The integral can be carried out analytically

$$\begin{aligned} 1 &= \frac{1}{N_D D} \frac{k_B T}{\pi \hbar^2} \sum_\alpha \sqrt{m_z^\alpha m_x^\alpha} \sum_{n_y} \ln[\exp(x - y) + 1]\big|_0^\infty \\ &= \frac{1}{N_D D} \frac{k_B T}{\pi \hbar^2} \sum_\alpha \sqrt{m_z^\alpha m_x^\alpha} \sum_{n_y} \ln[\exp(x) + 1]. \end{aligned} \tag{A15}$$

From this identity the chemical potential can be calculated.

Appendix C. Solution of the Poisson Equation

We now solve Equation (20): From the three equations (27)–(29)

$$V_T(y < 0) = c_1(y + D_G) - eU_G', \tag{A16}$$

$$V_T(0 < y < D) = -\frac{C}{2}y^2 + \alpha y + \beta, \tag{A17}$$

and

$$V_T(y > D) = c_2(y - D_{BG}) - eU_{BG}' \tag{A18}$$

one finds

$$V_T'(y < 0) = c_1, \tag{A19}$$

$$V_T'(0 < y < D) = -Cy + \alpha \tag{A20}$$

and

$$V_T'(y > D) = c_2. \tag{A21}$$

1. The matching condition $V_T(0^+) = V_T(0^-)$ leads to

$$c_1 D_G - eU_G' = \beta. \tag{A22}$$

2. The matching condition $V_T'(0^-)/V_T'(0^+) = \kappa_1$ leads to

$$c_1 = \kappa_1 \alpha. \tag{A23}$$

3. The matching condition $V_T(D^-) = V_T(D^+)$ leads to

$$-\frac{C}{2}D^2 + \alpha D + \beta = c_2(D - D_{BG}) - eU'_{BG} = -c_2 D_{Box} - eU'_{BG}. \tag{A24}$$

4. The matching condition $V_T'(D^+)/V_T'(D^-) = \kappa_2$ leads to

$$c_2 = \kappa_2(-CD + \alpha) = -\kappa_2 CD + \kappa_2 \alpha. \tag{A25}$$

Equations (A22)–(A25) constitute four inhomogeneous linear equations for the unknown variables c_1, α, β and c_2. Equations (A22) and (A23) allow for the elimination of c_1 to find β

$$\beta = \kappa_1 \alpha D_G - eU'_G. \tag{A26}$$

Equations (A24) and (A25) allow for the elimination of c_2

$$-\frac{C}{2}D^2 + \alpha D + \beta = -(-\kappa_2 CD + \kappa_2 \alpha)D_{Box} - eU'_{BG} = \kappa_2 CDD_{Box} - \kappa_2 D_{Box}\alpha - eU'_{BG}. \tag{A27}$$

Inserting β from (A26) yields

$$\begin{aligned} & -\frac{C}{2}D^2 + \alpha D + \kappa_1 \alpha D_G - eU'_G = \kappa_2 CDD_{Box} - \kappa_2 D_{Box}\alpha - eU'_{BG} \\ \Leftrightarrow \quad & [D + \kappa_2 D_{Box} + \kappa_1 D_G)]\alpha = \frac{C}{2}D^2 + \kappa_2 CDD_{Box} + e(U'_G - U'_{BG}). \end{aligned} \tag{A28}$$

It follows that

$$\alpha = \frac{CD^2/2 + \kappa_2 CDD_{Box} + e(U'_G - U'_{BG})}{D + \kappa_2 D_{Box} + \kappa_1 D_G}. \tag{A29}$$

We examine the curvature term $Cy^2/2$ in a SOIFET. Setting $y = 1$ nm and assuming weak doping $N_A = 10^{21}$ m^{-3} $= 10^{15}$ cm^{-3} $= 10^{-6}$ nm^{-3} it follows that

$$\begin{aligned} \frac{C}{2}y^z &= \frac{1}{4\pi\kappa_0}\frac{4\pi N_A e^2 y^2}{\kappa_{Si}} = 9 \times 10^9 \frac{Jm}{C^2}\frac{12.566 \times 10^{21}\text{m}^{-3}(1.6 \times 10^{-19}\text{C})^2 \times 10^{-18}\text{m}^2}{12.4} \\ &= \frac{9 \times 12.566 \times 1.6^2}{12.4} 10^{9+21-38-18}\frac{Jm}{C^2}\text{m}^{-1}C^2 = 23.3510^{-26}J = 2.335 \times 10^{-25}J \\ &= 1.46 \times 10^{-6}\text{eV}. \end{aligned} \tag{A30}$$

In a thin body ($D \leq$ 10nm) FD SOI-FET with weak doping, the curvature term can be neglected.

Appendix D. Analytical Approximations for the Barrier Haight and the Threshold Voltage

We derive Equations (36) and (42): The barrier height V_0 as calculated from (33). In the limit $C \to 0$ it results from Equation (33)

$$\begin{aligned} V_0 &= \frac{\alpha}{2}D + \beta = \frac{\alpha}{2}D + \kappa_1 \alpha D_G - eU'_G \\ &= \left(\frac{e(U'_G - U'_{BG})}{D + \kappa_2 D_{Box} + \kappa_1 D_G}\right)\left(\frac{D}{2} + \kappa_1 D_G\right) - eU'_G = e(U'_G - U'_{BG})A - eU'_G \\ &= (1 - A)(-eU_G + V_G^F) + A(-eU_{BG} + V_{BG}^F) \\ &= V_0^0 - (1 - A)(eU_G) \end{aligned} \tag{A31}$$

with

$$A = \frac{D/2 + \kappa_1 D_G}{D + \kappa_2 D_{Box} + \kappa_1 D_G} \tag{A32}$$

and

$$V_0^0 = (1-A)V_G^F + A(-eU_{BG} + V_{BG}^F) = V_G^F + A(V_{BG}^F - V_G^F - eU_{BG}). \tag{A33}$$

From

$$V_0(U_G^{th}) = \mu \tag{A34}$$

and the third line of (A31), one finds

$$\begin{aligned} & \mu = (1-A)\left(-eU_G^{th} + V_G^F\right) + A\left(-eU_{BG} + V_{BG}^F\right) \\ \Leftrightarrow \quad & eU_G^{th} = -\frac{\mu}{1-A} + V_G^F + \frac{A}{1-A}\left(-eU_{BG} + V_{BG}^F\right). \end{aligned} \tag{A35}$$

If $\kappa_2 D_{Box} \gg D, \kappa_1 D_G$ the parameter A is small, allowing a first order expansion in A

$$\begin{aligned} eU_G^{th} &\sim -\mu + V_G^F + A\left(-\mu - eU_{BG} + V_{BG}^F\right) \sim -\mu + V_G^F + \frac{D/2 + \kappa_1 D_G}{\kappa_2 D_{Box}}\left(-\mu - eU_{BG} + V_{BG}^F\right) \\ &= -\mu_G + \frac{D/2 + \kappa_1 D_G}{\kappa_2 D_{Box}}(-\mu_{BG} - eU_{BG}) \end{aligned} \tag{A36}$$

In the second step we take the limit $\kappa_2 D_{Box} \gg D/2, \kappa_1 D_G$, so that $A \sim D/2 + \kappa_1 D_G/(\kappa_2 D_{Box})$.

References

1. Eugster, C.C.; del Alamo, J. Tunneling spectroscopy of an electron waveguide. *Phys. Rev. Lett.* **1991**, *67*, 3586. [CrossRef] [PubMed]
2. Eugster, C.C.; del Alamo, J. Electron waveguide devices. *Superlattices Microstruct.* **1998**, *23*, 121–137.
3. van Wees, B.J.; van Houten, H.; Beenakker, C.W.J.; Williamson, J.G.; Kouwenhoven, L.P.; van der Marel C. T. Foxon, D. Quantized conductance of point contacts in a two-dimensional. *Phys. Rev. Lett.* **1988**, *60*, 848. [CrossRef] [PubMed]
4. Wharam, D.A.; Thornton, T.H.; Newbury, R.; Pepper, M.; Ahmed, H.; Frost, J.E.F.; Hasko, D.G.; Peacock, D.C.; Ritchie, D.A.; Jones, G.A.C. One-dimensional transport and the quantisation of the ballistic resistance. *J. Phys. C* **1988**, *21*, L209. [CrossRef]
5. Cheng, K.; Khakifirooz, A. Fully depleted SOI (FDSOI) technology. *Sci. China Inf. Sci.* **2016**, *59*, 61402. [CrossRef]
6. Pandey, A. Recent Trends in Novel Semiconductor Devices. *Silicon* **2022**. [CrossRef]
7. Nemnes, G.A.; Wulf, U.; Racec, P.N. Nano-transistors in the Landauer-Büttiker formalism. *J. Appl. Phys.* **2004**, *96*, 596–604. [CrossRef]
8. Nemnes, G.A.; Wulf, U.; Racec, P.N. Nonlinear I-V characteristics of nanotransistors in the Landauer-Büttiker formalism. *J. Appl. Phys.* **2005**, *98*, 084308. [CrossRef]
9. Wulf, U.; Kučera, J.; Richter, H.; Horstmann, M.; Wiatr, M.; Höntschel, J. Channel engineering for nanotransistors in a semiempirical quantum transport model. *Mathematics* **2017**, *5*, 68. [CrossRef]
10. Wulf, U. A One-Dimensional Effective Model for Nanotransistors in Landauer-Büttiker Formalism. *Micromachines* **2020**, *11*, 359. [CrossRef]
11. Horstmann, M.; Greenlaw, D.; Feudel, T.; Wei, A.; Frohberg, K.; Burbach, G.; Gerhardt, M.; Lenski, M.; Stephan, R.; Wieczorek, K.; et al. Sub-50 nm gate length SOI transistor development for high performance microprocessors. *Mater. Sci. Eng. B* **2004**, *114*, 3–8. [CrossRef]
12. Numata, T.; Irisawa, T.; Tezuka, T.; Koga, J.; Hirashita, N.; Usuda, K.; Toyoda, E.; Miyamura, Y.; Tanabe, A.; Sugiyama, N.; et al. Performance enhancement of partially and fully depleted strained-SOI MOSFETs. *IEEE Trans. Electron Devices* **2006**, *53*, 1030–1038. [CrossRef]
13. Fenouillet-Beranger, C.; Denormel, S.; Icard, B.; Boeuf, F.; Coignus, J.; Faynot, L.; Brevard, L.; Buj, C.; Soonekindt, C.; Todeschini, J.; et al. Fully-Depleted SOI Technology using High-K and Single-Metal Gate for 32 nm Node LSTP Applications featuring 0.179 μm^2 6T-SRAM bitcell. In Proceedings of the 2007 IEEE International Electron Devices Meeting (IEDM), Washington, DC, USA, 10–12 December 2007.
14. Fenouillet-Beranger, C.; Thomas, O.; Perreau, P.; Noel, J.P.; Bajolet, A.; Haendler, S.; Tosti, L.; Barnola, S.; Beneyton, R.; Perrot, C.; et al. Efficient Multi-VT FDSOI technology with UTBOX for low power circuit design. In Proceedings of the 2010 Symposium on VLSI Technology (VLSIT), Honolulu, HI, USA, 15–17 June 2010.

15. Cheng, K.; Khakifirooz, A.; Kulkarni, P.; Edge, L.F.; Reznicek, A.; Adam, T.; He, H.; Seo, S.C.; Kanakasabapathy, S.; Schmitz, S.; et al. Challenges and Solutions of Extremely Thin SOI (ETSOI) for CMOS Scaling to 22 nm Node and Beyond. *ECS Trans.* **2010**, *27*, 951. [CrossRef]
16. Liu, Q.; Monsieur, F.; Kumar, A.; Yamamoto, T.; Yagishita, A.; Kulkarnic, P.; Ponoth, S.; Loubet, N.; Cheng, K.; Khakifirooz, A.; et al. Impact of back bias on ultra-thin body and BOX (UTBB) devices. In Proceedings of the 2011 Symposium on VLSI Technology—Digest of Technical Papers, Kyoto, Japan, 14–16 June 2011.
17. Skotnicki, T. Competitive SOC with UTBB SOI. In Proceedings of the 2011 IEEE International SOI Conference (SOI), Tempe, AZ, USA, 3–6 October 2011.
18. Noel, J.; Thomas, O.; Jaud, M.A.; Weber, O.; Poiroux, T.; Fenouillet-Beranger, C.; Rivallin, P.; Scheiblin, P.; Andrieu, F.; Vinet, M.; et al. Multi-VT UTBB FDSOI Device Architectures for Low-Power CMOS Circuit. *IEEE Trans. Electron Divices* **2011**, *58*, 2473–2482. [CrossRef]
19. Doris, B.; DeSalvo, B.; Cheng, K.; Morin, P.; Vinet, M. Planar Fully-Depleted-Silicon-On-Insulator technologies: Toward the 28 nm node and beyond. *Solid-State Electron.* **2016**, *117*, 37–59. [CrossRef]
20. Venugopal, R.; Ren, Z.; Datta, S.; Lundstrom, M.S.; Jovanovic, D. Simulating quantum transport in nanoscale transistors: Real versus mode-space approaches. *J. Appl. Phys.* **2002**, *92*, 3730–3739. [CrossRef]
21. Venugopal, R.; Goasguen, S.; Datta, S.; Lundstrom, M.S. Quantum mechanical analysis of channel access geometry and series resistance in nanoscale transistors. *J. Appl. Phys.* **2004**, *95*, 292–305. [CrossRef]
22. Wang, J.; Polizzi, E.; Lundstrom, M. A three-dimensional quantum simulation of silicon nanowire transistors with the effective-mass approximation. *J. Appl. Phys.* **2004**, *96*, 2192–2203. [CrossRef]
23. Polizzi, E.; Abdallah, N.B. Subband decomposition approach for the simulation of quantum electron transport in nanostructures. *J. Comput. Phys.* **2005**, *202*, 150–180. [CrossRef]
24. Luisier, M.; Schenk, A.; Fichtner, W. Quantum transport in two- and three-dimensional nanoscale transistors: Coupled mode effects in the nonequilibrium Green's function formalism. *J. Appl. Phys.* **2006**, *100*, 043713. [CrossRef]
25. Vyurkov, V.; Semenikhin, I.; Filippov, S.; Orlikovsky, A. Quantum simulation of an ultrathin body field-effect transistor with channel imperfections. *Solid State Electron.* **2012**, *70*, 106–113 [CrossRef]
26. Chu, Y.; Sarangapani, P.; Charles, J.; Klimeck, G.; Kubis, T. Explicit screening full band quantum transport model for semiconductor nanodevices. *J. Appl. Phys.* **2018**, *123*, 244501. [CrossRef]
27. Chu, Y.; Lu, S.-C.; Chowdhury, N.; Povolotskyi, M.; Klimeck, G.; Mohamed, M.; Palacios, T. Superior Performance of 5-nm Gate Length GaN Nanowire nFET for Digital Logic Applications. *IEEE Electron. Device Lett.* **2019**, *40*, 874–877. [CrossRef]
28. Martinez, A.; Barker, J.R. Quantum Transport in a Silicon Nanowire FET Transistor: Hot Electrons and Local Power Dissipation. *Materials* **2020**, *13*, 3326. [CrossRef]
29. Sun, B.; Richstein, B.; Liebisch, P.; Frahm, T.; Scholz, S.; Trommer, J.; Mikolajick, T.; Knoch, J. On the Operation Modes of Dual-Gate Reconfigurable Nanowire Transistors. *IEEE Trans. Electron. Devices* **2021**, *68*, 3684–3689. [CrossRef]
30. Prakash, O.; Dabhi, C.K.; Chauhan, Y.S.; Amrouch, H. Transistor Self-Heating: The Rising Challenge for Semiconductor Testing. In Proceedings of the 2021 IEEE 39th VLSI Test Symposium (VTS), San Diego, CA, USA, 25–28 April 2021.
31. Liu, R.; Li, X.; Sun, Y.; Li, F.; Shi, Y. Thermal Coupling Among Channels and Its DC Modeling in Sub-7-nm Vertically Stacked Nanosheet Gate-All-Around Transistor. *IEEE Trans. Electron. Devices* **2021**, *68*, 6563–6570. [CrossRef]
32. Young, K.K. Short-channel effect in fully depleted SOI MOSFETs. *IEEE Trans. Electron. Devices* **1989**, *36*, 399–402. [CrossRef]
33. Yan, R.H.; Ourmazd, A.; Lee, K.F. Scaling the Si MOSFET: From bulk to SOI to bulk. *IEEE Trans. Electron. Devices* **1992**, *39*, 1704–1710. [CrossRef]
34. Tsormpatzoglou, A.; Dimitriadis, C.A.; Clerc, R.; Rafhay, Q.; Panannakakis, G.; Ghibaudo, G. Semi-Analytical Modeling of Short-Channel Effects in Si and Ge Symmetrical Double-Gate MOSFETs. *IEEE Trans. Electron. Devices* **2007**, *54*, 1943–1952. [CrossRef]
35. Mohammadi, H.; Abdullah, H.; Dee, V.F. A review on modeling the channel potential in multi-gate MOSFETs. *Sains Malays.* **2014**, *43*, 861–866.
36. Li, X.; Ma, L.; Ai, Y.; Han, W. From parabolic approximation to evanescent mode analysis on SOI MOSFET. *J. Semicond.* **2017**, *38*, 024005. [CrossRef]